Robust determination of the anisotropic polarizability of nanoparticles using coherent confocal microscopy

Brynmor J. Davis* and P. Scott Carney

The Beckman Institute for Advanced Science and Technology, University of Illinois at Urbana-Champaign, Urbana, Illinois 61801, USA
*Corresponding author: bryn@uiuc.edu

A coherent confocal microscope is proposed as a means to fully characterize the elastic scattering properties of a nanoparticle as a function of wavelength. Using a high numerical aperture lens, two-dimensional scanning, and a simple vector-beam shaper, the rank-2 polarizability tensor is estimated from a single confocal image. A method for computationally efficient data processing is described, and numerical simulations show that this algorithm is robust to noise and uncertainty in the focal plane position. The proposed method is a generalization of techniques that provide an estimate of a limited set of scattering parameters, such as a single orientation angle for rodlike particles. The measurement of the polarizability obviates the need for *a priori* assumptions about the nanoparticle. © 2008 Optical Society of America

OCIS codes: 100.3200, 110.1758, 120.5410, 180.3170, 290.0290.

1. INTRODUCTION

Nanoparticles are currently the subject of intense study in the scientific community [1,2] and are being used in fields as diverse as drug delivery [3], sensing [4], bioimaging [5], and sorbent manufacture [6]. Not least among the interesting properties of nanoparticles are their optical characteristics. The optical attributes of nanoparticles are observed in familiar materials, such as opal [7] and stained glass [8]. More recently the optical properties of intricate nanostructures have been exploited in the construction of metamaterials [9,10], in the subwavelength containment of fields using optical antennas [11], and as novel contrast mechanisms in optical microscopy [12]. With an increasing use of nanoparticles in optical applications, it is desirable to be able to characterize the optical response of a single nanoparticle. This paper focuses on the elastic scattering properties, which are determined by a wavelength-dependent linear polarizability tensor for sufficiently small nanoparticles. The polarizability of a nanoparticle is determined both by the constituent material and by the particle size and shape [13,14]. For a known material and geometry, the polarizability may be determined analytically [15] or by computational methods [16,17], however small deviations from the specified shape may introduce significant optical changes (see [18] for related measurements from nanoparticle arrays). In this paper a method is proposed for directly inferring the polarizability without prior assumptions about the scatterer.

The measurement scheme proposed is based on a coherent confocal microscope. Coherent microscopes use interference with a reference beam to holographically record data and hence acquire the phase of the measured field. While coherent microscopy predates the invention of the laser [19], modern bright and broadband sources have made spectrally sensitive coherent microscopy a common practical methodology. This is evidenced by the popularity of techniques, such as optical coherence tomography (OCT) [20,21]. In addition to collecting phase-sensitive data, a coherent microscope has the advantage of high sensitivity when compared to a traditional intensity-based system. As a result, coherent microscopy is suitable for true nanoimaging as demonstrated by results such as the interferometric detection of single viruses and gold particles as small as 5 nm [22].

In coherent microscopy, the optical source is usually split into a reference field and a field that is used to illuminate the sample. The light returned from the sample is combined with the reference field, and the interferometric features in the data are used for image formation. To exhibit interference, the returned light must be spectrally coherent with the reference field and at the same wavelength. This means that potentially useful signals from a nanoparticle, such as Raman-scattered [23], higher-harmonic [24], and/or fluorescent [25] light, are not detected. As a result, the coherent microscope described here is used to measure only the linear component of the nanoparticle polarizability and the three-dimensional position of the nanoparticle. Additionally, scattering from the nanoparticle is dependent on the background embedding material, the nanoparticle material, and the nanoparticle geometry. These effects cannot necessarily be distinguished from the measured polarizability alone.

Traditional microscopy and spectroscopy usually involve the formation of a scalar image on spatial and/or spectral axes. While this image is immediately useful in many applications, it is possible to design sensing systems that form nonscalar images and/or exploit less obvi-

ous relationships between the collected data and the imaged objects (see [26] for a comprehensive discussion). For example, in many modern microscopy and imaging systems data are collected as a function of polarization and/or scattering angle, e.g., [27–30]. Additionally, in some applications the object of interest may be represented by a small number of parameters that are estimated from the data with very high precision. In those cases, an image may be a very poor way to interpret the object as the small number of degrees of freedom are distributed over the many noisy pixels of the image. For example, in single molecule microscopy [25] the *a priori* knowledge that the object can be parameterized by the molecule location allows the molecule to be localized with a precision orders of magnitude better than the diffraction limit [31–33].

In this paper, the nanoparticle is parameterized by a linear polarizability tensor and a three-dimensional position. This description implies prior knowledge of the object, namely, that it is pointlike and has a fixed position. This prior knowledge is used in conjunction with the instrument sensitivity to the polarization and angular distribution of the scattered light. Scattering from larger structures may require a more complicated description. In addition, it is assumed that the nanoparticle is sufficiently well isolated so as to preclude interaction with other particles [34]. The particle polarizability is related to the data observed in a coherent microscope, and it is shown here that the polarizability can subsequently be inferred from the measured data.

The results presented in this paper build on work from a number of authors. The characteristics of light scattered from a nanoparticle depend on the particle size, shape, and orientation, a fact exploited in a number of microscopy modalities [35]. For example, the polarization of light scattered from nanoparticles has been used to identify the two-dimensional orientation of rodlike structures [36,37]. Illuminating nanoparticles with a tightly focused vector beam (i.e., a beam with a spatially varying polarization) results in incident light with a polarization dependent on the angle of incidence. A single confocal image formed with the scattered light can then be used to distinguish particle shapes and estimate a two-dimensional orientation angle for rodlike structures [38]. Recently this technique has been extended to interferometric confocal microscopy to provide an enhancement in sensitivity [39].

In [36–39] the measurement systems described are sensitive to a subset of nanoparticle shape features. Given a lexicon of nanoparticle shape(s), expected data may be calculated, which then may be matched to the observed data to estimate features. For example, given that the sample consists of nanorods oriented perpendicular to the optical axis, the data allow the estimation of the azimuthal orientation angle. In [39] it is suggested that it may not be necessary to assume that the nanorods are perpendicular to the optical axis, i.e., it is conjectured that the polar orientation may also be measured. The work presented here explores and expands upon this idea. Rather than assuming nanoparticle shape(s) *a priori*, it is assumed only that the particle is small enough to be characterized by a point polarizability. Particle orientation is then obtained by examining the principal axes of the es-

timated polarizability tensor. The shape of the nanoparticle may be correlated with the polarizability components along these principal axes as demonstrated in a related measurement technique based on polarimetric measurements over random rotations of the nanoparticle [40,41]. The work presented here shows that a high numerical aperture (NA) coherent confocal image formed using vector-beam illumination is sufficient to infer the polarizability up to a complex constant. That is, the linear scattering properties of the nanoparticle are measured without *a priori* assumptions regarding particle shape. In addition, the proposed system is robust to defocus, and the data processing algorithms are computationally inexpensive.

As mentioned above, the principal axes of the polarizability are related to the orientation of an asymmetric nanoparticle. The orientation of nanoparticles has been determined optically using both scattering and fluorescence measurements. The fluorescence intensity from a nanoparticle or single molecule is typically stronger than the comparable scattering signal [42] and is therefore less challenging to detect. Fluorescence-based orientation imaging systems provide a point of comparison for the scattering-based instrument described here. Like the scattering-based systems, fluorescence orientation imaging involves postulating a model describing the relevant nanoparticle optics and estimating the parameters of this model from observed data.

The power coupled into a fluorophore, and hence the fluorescence emission rate, are dependent on the orientation of the fluorophore and the direction of the exciting field. This measurable dependence has resulted in the development of a number of systems, where the polarization of the focused exciting field can be controlled [43–47]. By varying the exciting polarization [48] or the detected polarization direction [49], the orientation of the fluorophore can be determined. Alternatively, it is possible to find the fluorophore orientation by matching observations from high-angle excitation [50], high-angle detection [51], vector-beam excitation [52], aberrated [53], or defocused [54–56] data to those predicted for different orientations. Most fluorescence orientation imaging systems assume a dipole model for the fluorophore, although chirality [57] and nondipolar emission [58] have been measured.

While scattering is a coherent field-dependent phenomenon, fluorescence is an incoherent intensity-dependent effect. For a pointlike nanoparticle, scattering is defined by a rank-2 tensor relating the incident field to the scattered field while fluorescence is captured by a rank-4 tensor relating the incident intensity and polarization state to the emitted intensity and polarization state. This rank-4 tensor is related to optical intensity measurements (see the model derived in [59]) but, due to high dimensionality, is difficult to estimate. The assumption of a dipolar fluorophore allows simplification of the effective fluorescence tensor and makes fluorophore orientation characterization feasible. In this paper, it is shown that such simplifications are not necessary when estimating the rank-2 polarizability tensor that characterizes the linear nanoparticle scattering; the polarizability tensor is estimated from a single coherent confocal image.

In Section 2 a forward model for the coherent confocal

microscope is derived. In Section 3 this model is approximated in a manner that reduces the computational cost of the polarizability estimation. The procedure for estimating the polarizability is given in Section 4, i.e., the inverse problem is solved. The method is demonstrated and characterized by numerical experiments in Section 5, and conclusions are drawn in Section 6.

2. FORWARD MODEL

The instrument must be thoroughly modeled in order to determine the nanoparticle position and polarizability from the available data. This section describes the proposed instrument and the mathematical model and follows the coherent microscope treatment presented in [60].

As may be seen in Fig. 1, the proposed instrument consists of a Michelson interferometer coupled to an imaging system. A polychromatic stochastic reference field is focused into the object using a high NA lens and a vector-beam shaper. A single frequency-domain realization of the reference field is denoted by $\mathbf{E}^{(r)}(k)$ (where k is the wavenumber). The scattered field returned from the sample is denoted by $\mathbf{E}^{(s)}(\mathbf{r};k)$, where $\mathbf{r}$ denotes the position of the geometrical focus of the lens. The scattered field is added to the reference field and averaged at the detector. The data collected are thus proportional to the total spectral density

$$I(\mathbf{r};k) = \langle |\mu\mathbf{E}^{(r)}(k) + \mathbf{E}^{(s)}(\mathbf{r};k)|^2 \rangle,$$

$$= \langle |\mu\mathbf{E}^{(r)}(k)|^2 \rangle + 2\,\mathrm{Re}\{S(\mathbf{r};k)\} + \langle |\mathbf{E}^{(s)}(\mathbf{r};k)|^2 \rangle, \quad (1)$$
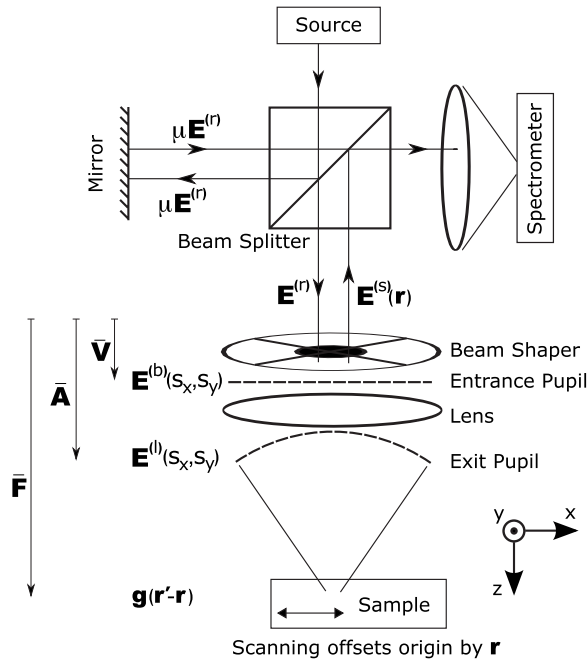

Fig. 1. Illustration of the proposed coherent confocal system including fields and tensor operators used in the model derivation. The reference field is denoted by $\mathbf{E}^{(r)}$, the field after the beam shaper by $\mathbf{E}^{(b)}$, the field after the lens by $\mathbf{E}^{(l)}$, the field in the sample by $\mathbf{g}$, and the backscattered field by $\mathbf{E}^{(s)}$. The tensor operators $\overline{\mathbf{V}}$, $\overline{\mathbf{A}}$, and $\overline{\mathbf{F}}$ give relations between the fields of interest. Note that the dependence on the wavenumber k has been dropped in the notation and that the tensor operators describe the evolution of fields in the direction of the arrows.

where μ is a constant that accounts for any depletion of the reference field and $\langle\cdot\rangle$ indicates an expected value. The interferometric cross term is

$$S(\mathbf{r};k) = \langle [\mu\mathbf{E}^{(r)}(k)]^\dagger \mathbf{E}^{(s)}(\mathbf{r};k) \rangle, \quad (2)$$

and † is the Hermitian transpose operator.

The first term in Eq. (1) is constant with $\mathbf{r}$ and can be removed (see [61] for a discussion of the effects of the noise associated with this first term). The third (autocorrelation) term is typically of much lower magnitude than the other two terms and is assumed to be negligible. Finally, the complex signal S can be recovered from the real signal. To avoid ambiguities in the phase, the reference arm delay must be shorter than the minimum travel time to the sample less the reciprocal of the source bandwidth. The imaginary part of the complex signal $S(\mathbf{r};k)$ may be obtained as the Hilbert transform of $\mathrm{Re}\{S(\mathbf{r};k)\}$ with respect to k [62,63]. This signal processing operation requires adequately sampled data collected over the full source bandwidth.

As shown in Fig. 1, the plane-wave reference field $\mathbf{E}^{(r)}$ falling on the vector-beam shaper produces a field $\mathbf{E}^{(b)}$ on the entrance pupil of the objective lens, and this field in turn maps to $\mathbf{E}^{(l)}$ on the exit pupil of the lens. Following standard practice [64], the vector-beam shaper and the objective lens are modeled within the accuracy of geometrical optics. Each ray emerging from the lens can be traced back to a point on the entrance pupil. In this case, an infinity-corrected aplanatic lens is assumed so that each (z-directed) ray passing through the beam shaper to the entrance pupil emerges at the same (x,y) location on the exit pupil.

The field $\mathbf{E}^{(b)}$ is determined by the illuminating reference field and a tensor operator $\overline{\mathbf{V}}$ representing the action of the beam shaper, i.e.,

$$\mathbf{E}^{(b)}(s_x,s_y;k) = \overline{\mathbf{V}}(s_x,s_y)\mathbf{E}^{(r)}(k). \quad (3)$$

Here the overbar indicates a tensor and, for simplicity, the beam shaper is assumed to be independent of k. The variables s_x and s_y refer to the x and y components of a unit vector directed from a point on the exit pupil toward the geometrical focus. The coordinates (s_x,s_y) may thus be considered the labels of particular geometric rays.

The vector-beam shaper is used to produce diversity in the polarization at the entrance pupil. An alternative approach would be to take multiple images with different illumination polarizations, however this would require additional collection time and coregistration between the collected images. In this paper a simple vector beam is proposed; a linearly polarized incident beam is partitioned into quadrants and half-wave plates are employed to rotate the polarization of the incident field. The resulting beam profile is illustrated in Fig. 2 and compared to a more traditional radially polarized beam. In both cases the center of the beam shaper is opaque and the action of the beam shaper is assumed to produce negligible deviation from the collimated propagation of the incident field. The simple beam shaper results in two quadrants that are x-polarized and two components that are y-polarized while the radially polarized beam achieves a smoothly varying polarization at the cost of increased experimental
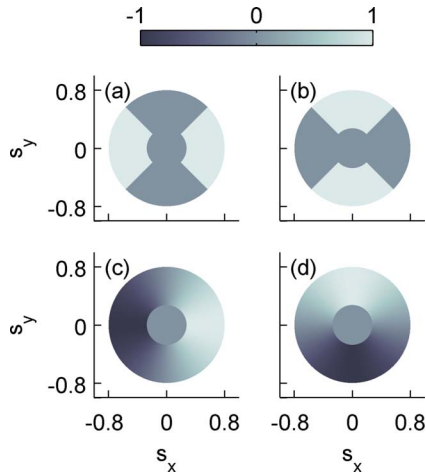
Fig. 2. (Color online) Fully polarized example fields at the entrance pupil, $\mathbf{E}^{(b)}$. The field direction is parallel to the entrance pupil with the (a),(c) x-polarized and (b),(d) y-polarized field components shown separately. (a),(b) The proposed beam is piecewise constant, providing a simplified experimental implementation compared to a more traditional (c),(d) radially polarized beam. The fields are displayed as a function of the cosines of the angles-to-focus over the 0.8 NA lens aperture.

complexity [43,44]. The comparison between the two beams seen in Fig. 2 is similar to the comparison between radial and pseudoradial beams presented in [65] except that opposing quadrants do not have opposing signs.

The mapping from $\mathbf{E}^{(b)}$ to $\mathbf{E}^{(l)}$ is given by a standard tensor operator obtained from simple rotations of Eq. (2.23) in [64]. The tensor operator $\overline{\mathbf{A}}$ contains this operation in addition to the action of the beam shaper so that the field at the lens exit pupil is

$$\mathbf{E}^{(l)}(s_x,s_y;k) = \overline{\mathbf{A}}(s_x,s_y)\mathbf{E}^{(r)}(k). \tag{4}$$

The field $\mathbf{E}^{(l)}$ for the example system is shown in Fig. 3 and is compared to a converging radially polarized field. It can be seen that the high NA (0.8) produces high angles-to-focus and hence significant z components in the electric field. Blocking the center of the beam shaper ensures that these z-polarized components can be made of a magnitude comparable to that of the x- and y-polarized components. It can be seen in Section 4 that the diversity of polarization at the exit pupil is critical in the estimation of the nanoparticle polarizability.

Each position on the exit pupil is associated with an angle-to-focus. This means that the field $\mathbf{E}^{(l)}$ can be regarded as an angular spectrum of the illuminating field at the focal plane [64]. With the geometrical focus at $\mathbf{r}$, the focused field at the point $\mathbf{r}'$ in the sample is given by the expression

$$\mathbf{g}(\mathbf{r}' - \mathbf{r};k) = \frac{k}{2\pi i}\int_\Omega ds_x ds_y \frac{\overline{\mathbf{A}}(s_x,s_y)\mathbf{E}^{(r)}(k)}{s_z(s_x,s_y)}e^{ik\mathbf{s}\cdot(\mathbf{r}'-\mathbf{r})},$$

$$= \overline{\mathbf{F}}(\mathbf{r}' - \mathbf{r};k)\mathbf{E}^{(r)}(k), \tag{5}$$

where

$$s_z(s_x,s_y) = \sqrt{1 - s_x^2 - s_y^2}, \tag{6}$$

$\mathbf{s}=(s_x,s_y,s_z)^T$ (T is the transpose operator), and integration is over the unit disk $\Omega=\{s_x,s_y:s_x^2+s_y^2<1\}$. Note that focusing into a sample with a background-index mismatch can also be described using a straightforward modification of this angular spectrum framework [66].

The exit pupil fields from Figs. 3(a)–3(c) produce the focused intensities seen in Fig. 4. As mentioned earlier, the beam focusing described here is similar to a pseudoradial beam [65] except that opposing quadrants in Figs. 2(a)

Fig. 4. (Color online) Calculated intensities of the focused example field $\mathbf{g}(x,y,z;k)$ at (a)–(c) $z=0$, (d)–(f) $z=\lambda$, and (g)–(i) $z=2\lambda$, where the wavelength is given by $\lambda=2\pi/k$. The intensities of each component are plotted separately, i.e., (a),(d),(g) $|g_x|^2$, (b),(e),(h) $|g_y|^2$, and (c),(f),(i) $|g_z|^2$ are shown in different plots.
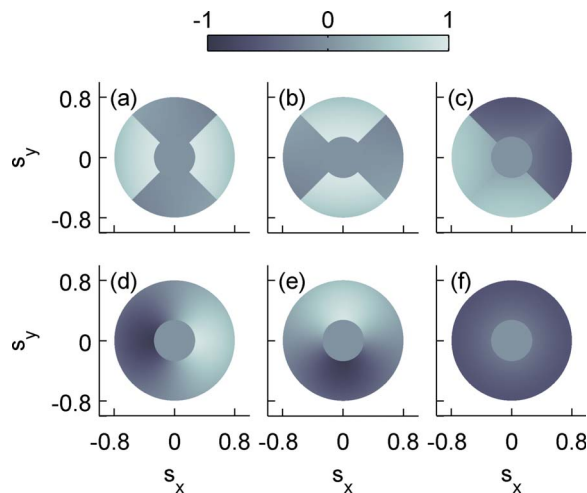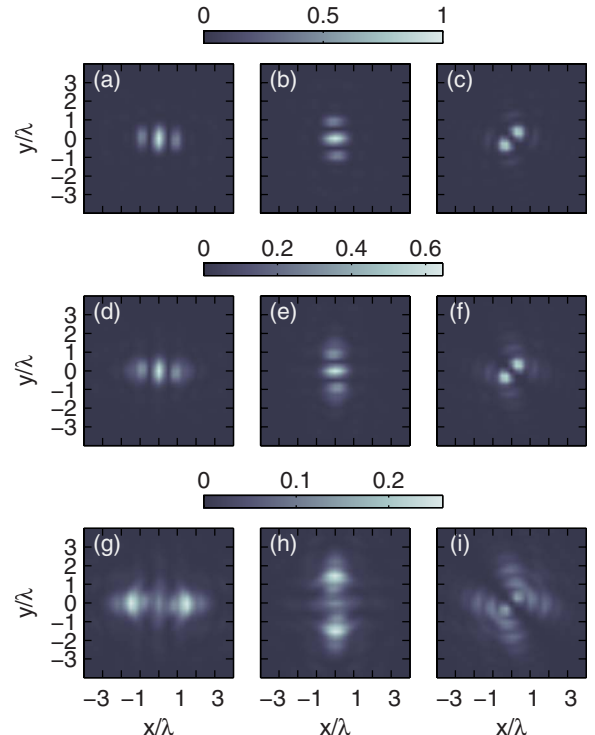

Fig. 3. (Color online) Fields at the exit pupil, $\mathbf{E}^{(l)}$, (a)–(c) for the proposed beam shape and (d)–(f) radially polarized system. The (a),(d) x-polarized, (b),(e), y-polarized, and (c),(f) z-polarized field components are shown separately. The field is displayed as a function of the cosines of the angles-to-focus over the 0.8 NA lens aperture.

and 2(b) do not have opposing signs. Field engineering approaches, such as radial beams, pseudoradial beams, and those mentioned in [45–47] provide physical manipulation of a vector beam to produce a desired polarization at focus. In this paper it is required only that the focal field consists of a spectrum of components with diverse polarization; the value of the resulting field at focus is not important. For example, in Fig. 4 it can be seen that the field at the geometrical focus has no z component while a focused pseudoradial beam produces a purely z-oriented field. The idea of polarization diversity is explored further in Section 4 when the tractability of the polarizability estimation problem is investigated as a function of NA and the beam shape.

The illuminating field interacts with a nanoparticle at position $\mathbf{r}^{(p)}$ with polarizability $\bar{\boldsymbol{\alpha}}(k)$. This produces a scattered field $k^2\bar{\boldsymbol{\alpha}}(k)\mathbf{g}(\mathbf{r}^{(p)}-\mathbf{r};k)$. This scattered light propagates back through the system to produce the field $\mathbf{E}^{(s)}$. Assuming that the lens and beam shaper obey reciprocity [67], the tensor operator $\overline{\mathbf{F}}^T$ describes propagation back through the system so that each realization of the backscattered field is given by the expression

$$\mathbf{E}^{(s)}(\mathbf{r};k) = k^2\overline{\mathbf{F}}^T(\mathbf{r}^{(p)}-\mathbf{r};k)\bar{\boldsymbol{\alpha}}(k)\mathbf{g}(\mathbf{r}^{(p)}-\mathbf{r};k). \qquad (7)$$

The complex data are then calculated by evaluating Eq. (2),

$$S(\mathbf{r};k) = \mu^* k^2$$
$$\times\langle[\mathbf{E}^{(r)}(k)]^\dagger\overline{\mathbf{F}}^T(\mathbf{r}^{(p)}-\mathbf{r};k)\bar{\boldsymbol{\alpha}}(k)\overline{\mathbf{F}}(\mathbf{r}^{(p)}-\mathbf{r};k)\mathbf{E}^{(r)}(k)\rangle. \qquad (8)$$

Due to the confocal nature of the system, the collected data are second-order in the focused field.

The focal point is scanned over two dimensions $\boldsymbol{\rho}$, where $\boldsymbol{\rho}=(x,y)^T$ and the focal plane is set to lie at $z=0$. Additionally, it is assumed that unmodeled instrument losses and uncertainties in the path lengths preclude precise knowledge of the absolute scale of the data. As a result, the data are written as

$$S(\boldsymbol{\rho};k) \propto \alpha_{\zeta\beta}(k)h_{\zeta\beta}(\boldsymbol{\rho}-\boldsymbol{\rho}^{(p)};z^{(p)},k), \qquad (9)$$

where the Einstein summation convention is applied over repeated subscripts and the point spread functions (PSFs) are

$$h_{\zeta\beta}(\boldsymbol{\rho};z^{(p)},k) = k^2 W_{\kappa\gamma}(k)F_{\beta\gamma}(-\boldsymbol{\rho},z^{(p)};k)F_{\zeta\kappa}(-\boldsymbol{\rho},z^{(p)};k), \qquad (10)$$

with the coherency matrix

$$\mathbf{W}(k) = \langle\mathbf{E}^{(r)}(k)[\mathbf{E}^{(r)}(k)]^\dagger\rangle \qquad (11)$$

defining the reference polarization state. From Eq. (9) it can be seen that each component of the polarizability (indexed by ζ and β) affects the data in a manner described by the PSF. These PSFs vary with $z^{(p)}$, the defocus of the nanoparticle.

Assuming an adequate sampling rate in $\boldsymbol{\rho}$, a sufficiently small sampling range to isolate a single nanoparticle and a sufficiently large sampling range to collect all relevant signals, Eq. (9) is rewritten in the Fourier domain as

$$\widetilde{S}(\mathbf{q};k) \propto \alpha_{\zeta\beta}(k)\widetilde{h}_{\zeta\beta}(\mathbf{q};z^{(p)},k)e^{-i\mathbf{q}\cdot\boldsymbol{\rho}^{(p)}}, \qquad (12)$$

where the tilde denotes a lateral Fourier transform.

The nanoparticle polarizability is estimated by optimally decomposing the data into a weighted sum of $h_{\zeta\beta}$ or $\widetilde{h}_{\zeta\beta}$ terms, where the weights give the elements of the polarizability. The coherent nature of the measurement means that the data are linear in the polarizability elements, which makes them easier to estimate than parameters such as orientation angles, which are nonlinear parameters of the data. Orientation parameters are estimated by nonlinear algorithms, such as pattern matching, e.g., [68]. It will be seen that the linear formulation of Eq. (12) allows efficient and stable estimation of the polarizability.

To estimate the elements of the polarizability $\alpha_{\zeta\beta}$, it is desirable that the PSF $h_{\alpha\beta}$ varies significantly with ζ and β. It can be seen from Eq. (10) that the PSFs are invariant to a reordering of ζ and β. This does not cause a problem as the polarizability is transpose symmetric by time reversal symmetry arguments [69] so that $\alpha_{\zeta\beta}=\alpha_{\beta\zeta}$. That is, the instrument produces six independent PSFs, and the polarizability is defined by six corresponding elements. The data are analyzed in the Fourier domain because, as shown in Section 3, a Fourier-domain representation allows a simplifying approximation. The Fourier-domain representations of the PSFs are calculated as follows.

At a given constant-z plane and wavenumber, the lateral Fourier transforms of the illuminating field components are found from the representation of Eq. (5). Specifically,

$$\widetilde{F}_{\beta\gamma}(\mathbf{q};z,k) = \frac{2\pi}{ik}\frac{A_{\beta\gamma}(\mathbf{q}/k)}{s_z(\mathbf{q}/k)}e^{iks_z(\mathbf{q}/k)z} \qquad (13)$$

expresses the Fourier optics relation between the focused field and the field emerging from the lens. The PSFs are the weighted sum of the products of $F_{\beta\gamma}$ components [Eq. (10)], and in the Fourier domain these products become convolutions so that

$$\widetilde{h}_{\zeta\beta}(-\mathbf{q};z^{(p)},k) = -4\pi^2 W_{\kappa\gamma}(k)\int_{\mathbb{R}^2}\mathrm{d}^2q' \frac{A_{\beta\gamma}\left(\dfrac{\mathbf{q}-\mathbf{q}'}{k}\right)A_{\zeta\kappa}\left(\dfrac{\mathbf{q}'}{k}\right)}{s_z\left(\dfrac{\mathbf{q}-\mathbf{q}'}{k}\right)s_z\left(\dfrac{\mathbf{q}'}{k}\right)}$$
$$\times\exp\left\{ik\left[s_z\left(\frac{\mathbf{q}-\mathbf{q}'}{k}\right)+s_z\left(\frac{\mathbf{q}'}{k}\right)\right]z^{(p)}\right\}. \qquad (14)$$

These expressions were evaluated for the example system on the focal plane ($z^{(p)}=0$), and the resulting Fourier spectra are shown in Fig. 5. The exit pupil fields of Figs. 3(a)–3(c) are related to these plots using Eqs. (4), (11), and (14).

3. APPROXIMATE FORWARD MODEL

The data expected from a given nanoparticle are described by Eq. (12), where the Fourier-domain PSFs are calculated using Eq. (14). The Fourier-domain PSFs de-
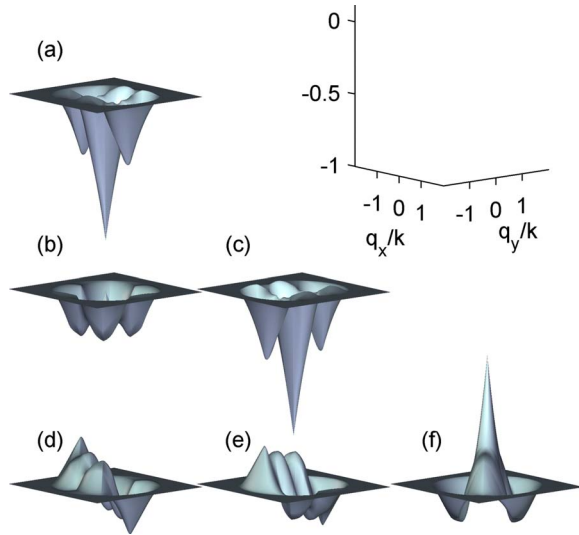
Fig. 5. (Color online) Fourier-domain representations of the focal plane PSFs for the example system. At $z^{(p)}=0$ and for this system, these functions are real. The function axes are shown in the upper right and the remaining plots show (a) $\tilde{h}_{xx}$, (b) $\tilde{h}_{xy}$, (c) $\tilde{h}_{yy}$, (d) $\tilde{h}_{xz}$, (e) $\tilde{h}_{yz}$, and (f) $\tilde{h}_{zz}$.

pend on k via simple axes scaling but depend on the nanoparticle defocus $z^{(p)}$ in a more complicated fashion. As will be seen in Section 4, it is necessary to calculate the PSFs at multiple values of $z^{(p)}$ in order to estimate the nanoparticle polarizability. For this reason Eq. (14) will be approximated in a manner that makes numerical evaluation inexpensive in terms of both computations and memory requirements.

Due to the finite extent of $\overline{\mathbf{A}}$, the integrand of Eq. (14) is nonzero only on a circle with a radius of twice the NA. Within this area the magnitude of the integrand is peaked at N points $\mathbf{q}'=\mathbf{p}(\mathbf{q};\zeta,\beta,n)$, where $n=1,\dots,N$. The region of integration is divided into N regions $R(\mathbf{q};\zeta,\beta,n)$ based on these peaks. For low $kz^{(p)}$ the exponential factor in Eq. (14) is approximated as constant in each region $R(\mathbf{q};\zeta,\beta,n)$, resulting in

$$\tilde{h}_{\zeta\beta}(-\mathbf{q};z^{(p)},k) \approx -4\pi^2\sum_{n=1}^{N}\exp\left\{iks_z\left(\frac{\mathbf{p}(\mathbf{q};\zeta,\beta,n)}{k}\right)z^{(p)}\right\}$$
$$\times\exp\left\{iks_z\left(\frac{\mathbf{q}-\mathbf{p}(\mathbf{q};\zeta,\beta,n)}{k}\right)z^{(p)}\right\}W_{\kappa\gamma}(k)$$
$$\times\int_{R(\mathbf{q};\zeta,\beta,n)}\mathrm{d}^2q'\frac{A_{\beta\gamma}\left(\frac{\mathbf{q}-\mathbf{q}'}{k}\right)A_{\zeta\kappa}\left(\frac{\mathbf{q}'}{k}\right)}{s_z\left(\frac{\mathbf{q}-\mathbf{q}'}{k}\right)s_z\left(\frac{\mathbf{q}'}{k}\right)}.$$
(15)

For the fully polarized example considered here, the integral under consideration depends on the overlap between offset copies of the patterns shown in Figs. 3(a)–3(c). For this example it can be seen that the integrand generally has one dominant peak at $\mathbf{p}(\mathbf{q};\zeta,\beta,1)$ or, when $\zeta=\beta$,

two equally dominant peaks, where $\mathbf{p}(\mathbf{q};\zeta,\beta,2)$ $=\mathbf{q}-\mathbf{p}(\mathbf{q};\zeta,\beta,1)$. In either of these cases Eq. (15) reduces to

$$\tilde{h}_{\zeta\beta}(-\mathbf{q};z^{(p)},k) \approx -4\pi^2\exp\left\{iks_z\left(\frac{\mathbf{p}(\mathbf{q};\zeta,\beta,1)}{k}\right)z^{(p)}\right\}$$
$$\times\exp\left\{iks_z\left(\frac{\mathbf{q}-\mathbf{p}(\mathbf{q};\zeta,\beta,1)}{k}\right)z^{(p)}\right\}$$
$$\times W_{\kappa\gamma}(k)\int_{\mathbb{R}^2}\mathrm{d}^2q'\frac{A_{\beta\gamma}\left(\frac{\mathbf{q}-\mathbf{q}'}{k}\right)A_{\zeta\kappa}\left(\frac{\mathbf{q}'}{k}\right)}{s_z\left(\frac{\mathbf{q}-\mathbf{q}'}{k}\right)s_z\left(\frac{\mathbf{q}'}{k}\right)},$$
(16)

where in the two peak cases the fact that the exponential prefactors are equal for $\mathbf{p}(\mathbf{q};\zeta,\beta,1)$ and $\mathbf{p}(\mathbf{q};\zeta,\beta,2)$ has been exploited. This equation can be written in the simple form

$$\tilde{h}_{\zeta\beta}(-\mathbf{q};z^{(p)},k) \approx H(\mathbf{q};\zeta,\beta,k)e^{ik\Phi(\mathbf{q};\zeta,\beta,k)z^{(p)}},\quad (17)$$

where the Fourier transforms of the PSFs for an in-focus particle ($z^{(p)}=0$) are

$$H(\mathbf{q};\zeta,\beta,k) = -4\pi^2 W_{\kappa\gamma}(k)\int_{\mathbb{R}^2}\mathrm{d}^2q'\frac{A_{\beta\gamma}\left(\frac{\mathbf{q}-\mathbf{q}'}{k}\right)A_{\zeta\kappa}\left(\frac{\mathbf{q}'}{k}\right)}{s_z\left(\frac{\mathbf{q}-\mathbf{q}'}{k}\right)s_z\left(\frac{\mathbf{q}'}{k}\right)},$$
(18)

and defocus contributes a phase term of the form

$$\Phi(\mathbf{q};\zeta,\beta,k) = s_z\left(\frac{\mathbf{q}-\mathbf{p}(\mathbf{q};\zeta,\beta,1)}{k}\right)+s_z\left(\frac{\mathbf{p}(\mathbf{q};\zeta,\beta,1)}{k}\right).$$
(19)

The approximation, Eq. (17), allows an easy calculation of the system PSFs as a function of the nanoparticle defocus $z^{(p)}$. Within the bounds of this approximation, it is possible to calculate the PSFs at any plane using simple manipulations of H and Φ. These functions vary trivially with k, so it is only necessary to store 12 two-dimensional images (i.e., functions of $\mathbf{q}$) in order to calculate the six PSFs required to characterize the system.

The approximation described in this section can be tested by evaluating Eq. (14) and examining the behavior of the magnitude and phase across multiple values of $z^{(p)}$. According to Eq. (17) the resulting magnitude should not change with $z^{(p)}$. The magnitudes calculated for this example are shown in Fig. 6, and it can be seen that they are relatively stable with up to a wavelength of defocus. The corresponding phase profiles are shown in Fig. 7, although it should be noted that the $z^{(p)}=0$ column of Fig. 6 has been replaced with $z^{(p)}=\lambda/4$ since the in-focus spectra are real and therefore have no useful phase profile. The images in Fig. 7 are plotted on a scale proportional to $z^{(p)}$ so that the along-row consistency corresponds to a phase profile scaling with $z^{(p)}$ as required by Eq. (17). Taken to-
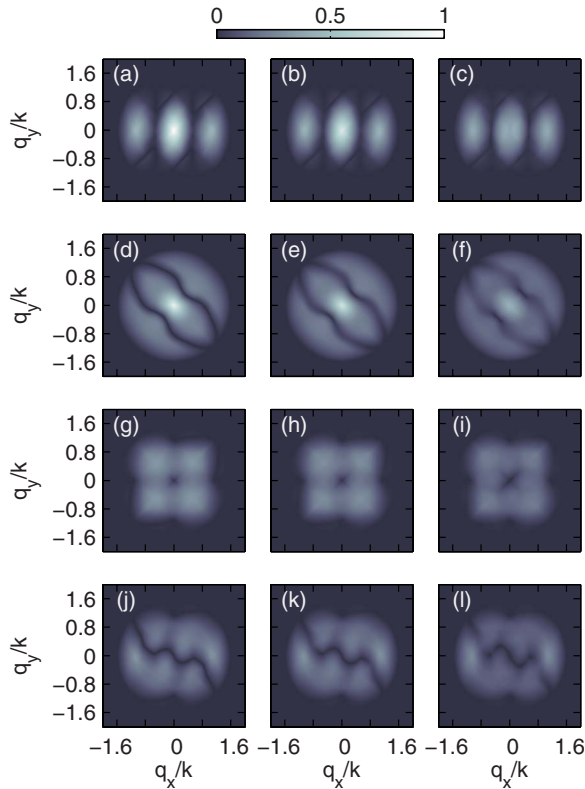
Fig. 6. (Color online) Fourier-domain magnitudes of the system PSFs at (a),(d),(g),(j) $z^{(p)}=0$, (b),(e),(h),(k) $z^{(p)}=\lambda/2$, and (c),(f),(i),(l) $z^{(p)}=\lambda$. Magnitudes for (a)–(c) $\widetilde{h}_{xx}$, (d)–(f) $\widetilde{h}_{zz}$, (g)–(i) $\widetilde{h}_{xy}$, and (j)–(l) $\widetilde{h}_{xz}$ are shown with $\widetilde{h}_{yy}$ being a rotation of $\widetilde{h}_{xx}$ and $\widetilde{h}_{yz}$ being a rotation of $\widetilde{h}_{xz}$. Note that the first column represents the magnitudes of the plots shown in Fig. 5.
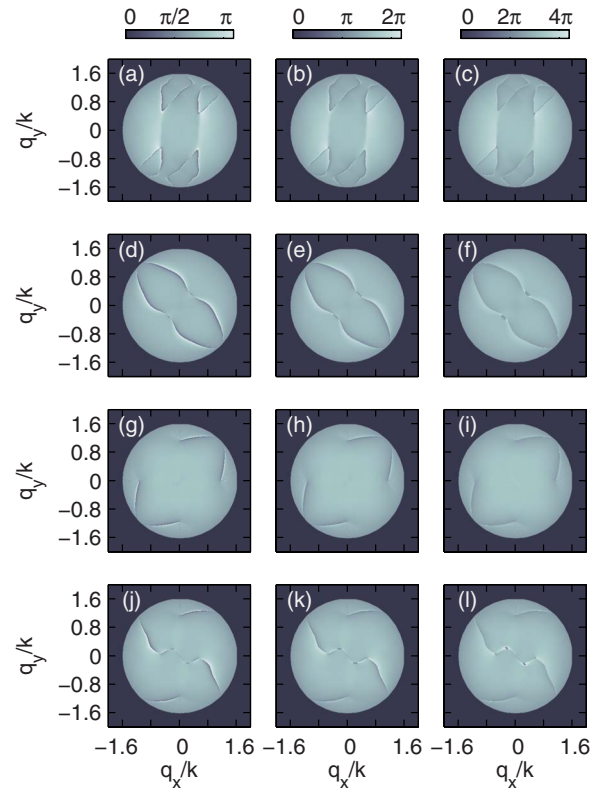

Fig. 7. (Color online) Fourier-domain phase profiles of the system PSFs at (a),(d),(g),(j) $z^{(p)}=\lambda/4$, (b),(e),(h),(k) $z^{(p)}=\lambda/2$, and (c),(f),(i),(l) $z^{(p)}=\lambda$. These are calculated by dividing $\widetilde{h}$ at $z^{(p)}$ into $\widetilde{h}$ at $z^{(p)}=0$ and taking the complex angle. Phases for (a)–(c) $\widetilde{h}_{xx}$, (d)–(f) $\widetilde{h}_{zz}$, (g)–(i) $\widetilde{h}_{xy}$, and (j)–(l) $\widetilde{h}_{xz}$ are shown with $\widetilde{h}_{yy}$ being a rotation of $\widetilde{h}_{xx}$ and $\widetilde{h}_{yz}$ being a rotation of $\widetilde{h}_{xz}$. Note that the phase profiles have been unwrapped and that the color scale varies across the columns.

gether, Figs. 6 and 7 indicate that the approximation derived in this section is relatively accurate up to at least a wavelength of defocus.

4. INVERSE PROBLEM

With a forward model formulated, the inverse problem can be addressed. That is, the nanoparticle parameters can be estimated from the collected data. The inverse problem is solved by comparing the observed data to data predicted using the forward model and a given set of nanoparticle parameters. The set of parameters giving the minimum discrepancy is chosen as estimated particle characteristics. Mathematically, a cost function is defined as

$$C[\bar{\boldsymbol{\alpha}}(k),\mathbf{r}^{(p)};k] = \|\widetilde{S}(\mathbf{q};k) - \alpha_{\zeta\beta}(k)\widetilde{h}_{\zeta\beta}(\mathbf{q};z^{(p)},k)e^{-i\mathbf{q}\cdot\boldsymbol{\rho}^{(p)}}\|^2$$

(20)

and minimized with respect to $\mathbf{r}^{(p)}$ and $\bar{\boldsymbol{\alpha}}(k)$ at each k value. A Euclidean (i.e., ℓ^2) norm $\|\cdot\|$ is chosen in Eq. (20), which is consistent with a Gaussian noise model and maximum likelihood parameter estimation [70]. This noise model is consistent with interferometer measurements dominated by noise from the reference beam and/or thermal detector noise [61].

The Fourier-domain PSFs $\widetilde{h}$ used in Eq. (20) are calculated using either the unapproximated Eq. (14) or the ap-

proximate Eq. (17). The approximate calculation is more efficient and allows the precalculation of H and Φ. To find H, Eq. (18) is numerically evaluated. Rather than finding Φ by direct evaluation of Eq. (19) (which involves defining many peaks $\mathbf{p}$), a more simple approach is suggested by examination of Eq. (17). The exact Fourier spectra are calculated [using Eq. (14)] for a small value of $z^{(p)}$, divided by the spectra H, and finally the complex angle of the result is divided by $kz^{(p)}$ to obtain Φ.

Regardless of how the PSFs are calculated, the forward model [Eq. (12)] is linear in the polarizability elements due to the coherent nature of the measurements. Consequently, the elements of the polarizability are coefficients of the Fourier-domain PSFs in the expected data. The Fourier-domain PSFs essentially act as basis functions in an alternative data-space representation of the polarizability. The conditioning of a projection onto this basis determines the expected performance of the polarizability estimation procedure [i.e., the minimization of Eq. (20) with respect to $\bar{\boldsymbol{\alpha}}$] with dissimilar PSFs giving distinct signatures for each polarizability element and a more accurate estimate. This idea is explored in Fig. 8, where the conditioning is calculated as a function of NA. Quantification of the conditioning is based on the linear operator taking the six independent polarizability elements to the expected observed data; the ratio of the minimum eigen-
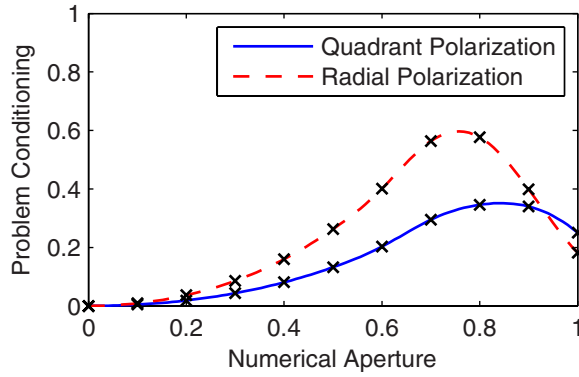
Fig. 8. (Color online) Conditioning of the relation between the polarizability elements and the collected data for various values of NA. Higher conditioning gives better estimation of the polarizability. Results for both the proposed quadrant-based beam and a radially polarized beam are plotted. In both cases the center of the beam is blocked as seen in Fig. 3. The diameter of the central blocked region scales with NA.

value of this operator to the maximum eigenvalue is plotted in Fig. 8. In the optimal case all eigenvalues would be equal giving a conditioning of 1 while a conditioning of 0 indicates a nullspace in the operator and unobservable polarizability components.

From Fig. 8 it can be seen that the tractability of the polarizability estimation problem generally improves with NA. This can be attributed to the fact that higher apertures produce more significant z-polarized fields and thus more fully probe the scattering properties. At very high NA the z-polarized field components exceed the x- and y-polarized components (which are limited by the central beam block) resulting in a detrimental effect on the conditioning. It can also be seen that the quadrant-based beam proposed here does not perform as well as a radially polarized beam. However, the proposed system can be more easily implemented experimentally and, as shown in Section 5, can still be expected to give high-fidelity estimates of the polarizability. As a point of comparison, an x-polarized plane wave incident on an unapodized aplanatic lens of unity NA produces very low-level y-polarized field components and gives a conditioning of less than 0.02.

The cost at fixed position $\mathbf{r}^{(p)}$ can be minimized with respect to the polarizability $\bar{\alpha}$ using a standard closed-form least-squares solution. Therefore, the cost at a given k is easily reduced to a nonlinear function of $\mathbf{r}^{(p)}$, where each value of $\mathbf{r}^{(p)}$ has an optimal polarizability associated with it. This three-dimensional nonlinear cost function can be minimized by standard optimization algorithms such as the Nelder–Mead simplex method [71,72]. This algorithm is used in the simulations presented in Section 5. In the Nelder–Mead method a simplex, in this case defined by four points in three-dimensional space, defines a volume in search space. The cost is evaluated at each of these points, and the points are iterated until a local minimum is contained within a small simplex volume. The initial simplex should be made large enough to include all reasonable nanoparticle positions. The approximation of Eq. (17) makes the evaluation of the cost inexpensive and the Nelder–Mead algorithm fast. Once a minimizing value for

$\mathbf{r}^{(p)}$ has been found, the corresponding minimizing polarizability (used in the evaluation of the cost at $\mathbf{r}^{(p)}$) completes the estimation of the nanoparticle parameters.

The inversion procedure described above is for a fixed value of k. To calculate the wavelength dependence of the polarizability, the inversion can be performed over the full range of the wavenumber. However, the position of the nanoparticle does not vary with k and so the optimal position found at the first inversion calculation is valid over all k. Consequently, once the inversion is performed for one value of k, the position $\mathbf{r}^{(p)}$ is known and the polarizability $\bar{\alpha}(k)$ can be found for all other values of k by a standard least-squares minimization of Eq. (20) with $\mathbf{r}^{(p)}$ fixed. The iterative inversion need be performed only once.

While the instrument shown in Fig. 1 can be regarded as an imaging system collecting data over spatial and spectral axes, the determination of the nanoparticle parameters is not traditional imaging. A meaningful two- or three-dimensional function, describing density or structure, is not the objective, rather a tensor and a vector are estimated from the data. The *a priori* knowledge that the object is characterized by these parameters results in a well-posed inverse problem, provided that there is sufficient diversity in the responses from the polarizability elements (see Fig. 8).

5. SIMULATIONS

Numerical simulations were used to investigate the performance of the proposed system. Synthetic data were generated using Eqs. (9) and (10). Complex white Gaussian noise was added to these data and the parameters of the nanoparticle estimated according to the method described in Section 4. By comparing the parameter estimates to those used to generate the data, the expected performance may be quantified. The simulations presented are at a single wavenumber as the system is not coupled across k. That is, the nanoparticle polarizability and position are estimated at a single value of k with the understanding that the spectral dependence of the polarizability could then be easily calculated from images collected at other wavelengths.

To calculate synthetic data, the focused field must be found. The inversion procedure is defined in the Fourier domain and depends directly on the exit pupil fields $\mathbf{E}^{(l)}$ shown in Figs. 3(a)–3(c). To avoid an artificial match between the forward model and the inverse processing, it is not desirable to calculate the focused field $\mathbf{g}$ using numerical methods that start with $\mathbf{E}^{(l)}$, e.g., [73,74]. Instead the focal field was calculated using the approach outlined in [46], where $\mathbf{E}^{(l)}$ is decomposed into a series expansion with each term being analytically propagated into the sample. The resulting calculation involves the evaluation of one-dimensional integrals as in [64] but with higher order Bessel functions included in the integrands. This method was used to calculate the fields shown in Fig. 4.

Nanoparticle parameters used in the simulations were generated randomly. A polarizability was constructed by

first using manipulations of a random number generator to give a random complex orthonormal spatial basis $\boldsymbol{v}^{(j)}$, where $j = 1, 2, 3$. Three unit-variance zero-mean complex scalars $c^{(j)}$ were generated, and the polarizability is thus given by

$$\bar{\boldsymbol{\alpha}} = [\boldsymbol{v}^{(j)}]^T c^{(j)} \boldsymbol{v}^{(j)}. \tag{21}$$

This method of constructing $\bar{\boldsymbol{\alpha}}$ guarantees a symmetric polarizability as physically required. A typical example of a random polarizability is

$$\bar{\boldsymbol{\alpha}} = \begin{bmatrix} 0.433 + 0.633i & 0.137 - 0.380i & -0.308 - 0.424i \\ 0.137 - 0.380i & -0.540 + 0.164i & -0.096 - 0.293i \\ -0.308 - 0.424i & -0.096 - 0.293i & -0.087 + 0.185i \end{bmatrix}, \tag{22}$$

where $\bar{\boldsymbol{\alpha}}$ is represented as a matrix operating on vectors in Cartesian coordinates.

The location of the nanoparticle was also randomly generated. The values $x^{(p)}$ and $y^{(p)}$ were both normally distributed about 0 with a standard deviation equal to the wavelength λ. The axial offset $z^{(p)}$ has a standard deviation of $\lambda/5$ and in different simulations was given various means in order to examine how the approximation of Eq. (17) affects performance as a function of expected defocus. An example position for the case where $\langle z^{(p)} \rangle = 0$ is

$$\mathbf{r}^{(p)} = \lambda \begin{bmatrix} -1.67 & -1.24 & -0.088 \end{bmatrix}^T. \tag{23}$$

Complex white Gaussian noise was added to the data, and the signal-to-noise ratio (SNR) is defined as the ratio of the noise variance and the expected square magnitude

of the data from a random scatterer placed at the geometrical focus. Synthetic data at various SNRs are shown in Fig. 9 for a nanoparticle with parameters given by Eqs. (22) and (23). The focus is scanned in steps of $\lambda/4$ in both the x and y directions.

The nanoparticle position and polarizability were estimated according to the procedure described in Section 4 with the approximate model used for PSF calculation. As mentioned in Section 2, the absolute magnitude and phase of the polarizability are not easily measurable. Consequently the estimated polarization is scaled by a constant to give a minimum difference with actual polarization when making comparisons between the two. The 14.3 dB SNR data produced from the example nanoparticle parameters are inverted to give parameter estimates of

$$\hat{\bar{\boldsymbol{\alpha}}} = \begin{bmatrix} 0.417 + 0.622i & 0.137 - 0.401i & -0.339 - 0.405i \\ 0.137 - 0.401i & -0.543 + 0.170i & -0.031 - 0.279i \\ -0.339 - 0.405i & -0.031 - 0.279i & -0.111 + 0.168i \end{bmatrix} \tag{24}$$

and

$$\hat{\mathbf{r}} = \lambda \begin{bmatrix} -1.66 & -1.25 & -0.085 \end{bmatrix}^T. \tag{25}$$

It can be seen that these estimates show good fidelity with the original parameters.

The Nelder–Mead algorithm was implemented using the FMINSEARCH function in the MATLAB 7.4 (Mathworks, Natick, Massachusetts) software package. This function requires an initialization point, which was found by normalizing the Fourier-domain data $\tilde{S}$ to unit magnitude, taking the inverse Fourier transform, and setting the initial value of $(x^{(p)}, y^{(p)})$ to the lateral position of the maximum-magnitude pixel. This approach is based on the phase correlation image registration technique [75]. The initial value of $z^{(p)}$ is set to zero.

The action of the estimation processing can also be examined in the Fourier domain. In Fig. 10 the Fourier-domain data can be seen (both noise-free and at the 14.3 dB SNR noise level) along with the data correspond-
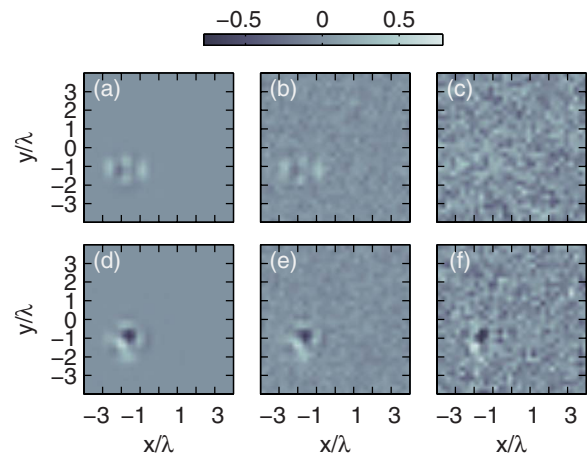

Fig. 9. (Color online) Simulated data for the example nanoparticle parameters of Eqs. (22) and (23). The (a)–(c) real and (d)–(f) imaginary parts of the data are plotted with (a),(d) no noise, (b),(e) SNRs of 14.3 dB, and (c),(f) 5.3 dB.
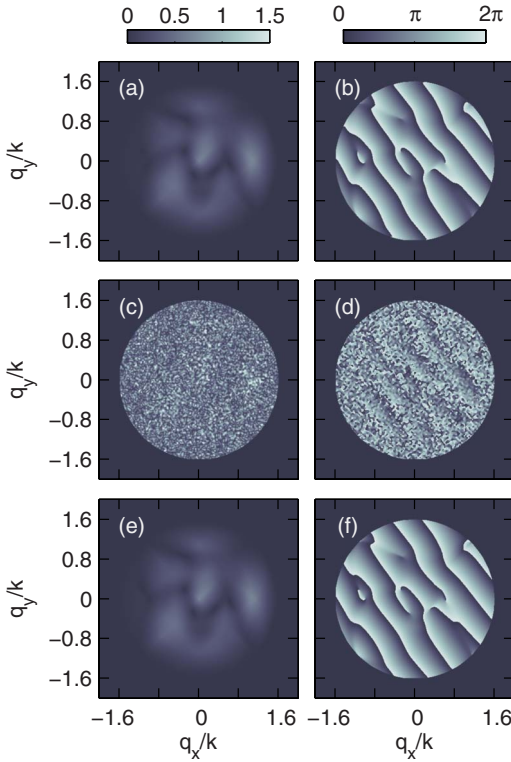
Fig. 10. (Color online) (a), (c), (e) Fourier-domain magnitudes and (b),(d),(f) phases of simulated data. (a),(b) Noise-free and (c),(d) 14.3 dB SNR data from the example nanoparticle parameters of Eqs. (22) and (23) are shown along with (e),(f) data corresponding to the parameters of Eqs. (24) and (25), which were estimated from the noisy data. Note that noise outside the system band limit ($q = 1.6$) is not shown and that approximately 0.25% of the pixels in plot (c) saturate the color scale.

ing to the estimated parameters. The similarity between the actual data and the estimated data indicates a small value of the cost function [Eq. (20)]. The plots seen in Fig. 10 are of high resolution, corresponding to a relatively large spatial data collection area of $30\lambda \times 30\lambda$. This range is chosen for display purposes; a smaller range can be used provided that all significant signals are collected.

The numerical experiment described above was repeated at different noise levels and different values of expected defocus $\langle z^{(p)} \rangle$, giving the results seen in Fig. 11. The quality of each polarizability and position estimate is assigned a quantitative metric; for the position estimate the metric is the ℓ^2 norm of the position error, and for the polarizability the metric is the ℓ^2 norm of the polarizability error (arranged as a 9×1 vector) divided by the ℓ^2 norm of the polarizability. For the example random polarizability [Eq. (22)] and its estimate [Eq. (24)] this error metric is 0.0823 while for the example location [Eq. (23)] and location estimate [Eq. (25)] the error metric is 0.0103λ. Note that the estimated polarizability is scaled by a constant (accounting for unknown instrument phase and amplitude) to give the minimum error, which means that the maximum realizable polarizability error metric is 1 (achieved for a scale factor of 0).

From Fig. 11 it can be seen that the reconstruction quality decreases with higher noise levels and also with the expected defocus. The degradation with $\langle z^{(p)} \rangle$ can be attributed to the approximation of Section 3 breaking
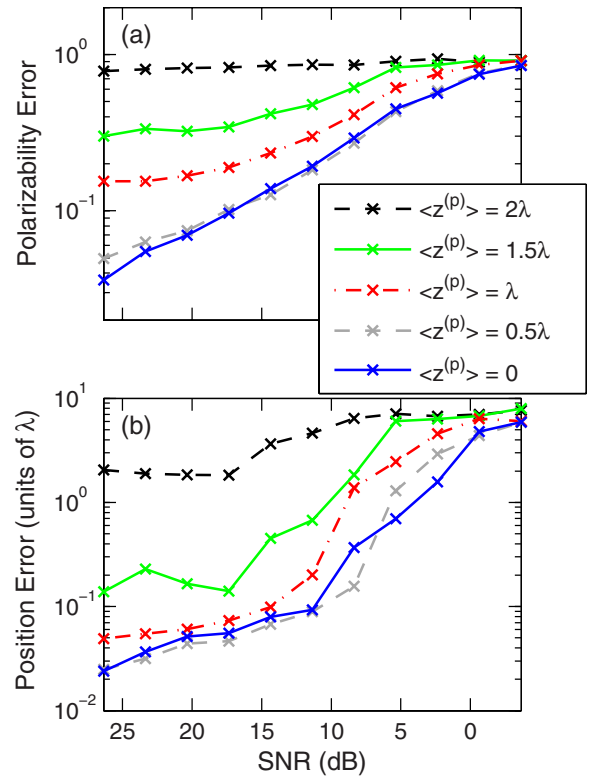

Fig. 11. (Color online) (a) Average polarizability and (b) position errors for various SNRs and expected nanoparticle distances from focus. Each marked point is calculated from 100 simulations and each simulation has a different random nanoparticle polarizability, nanoparticle location, and noise realization.

down. In terms of the reconstruction quality, the approximation deteriorates around $\pm\lambda$ of defocus and is invalid beyond $\pm2\lambda$.

6. CONCLUSIONS

It was shown that spectrally sensitive, two-dimensionally scanning, coherent confocal microscopes (e.g., Fourier-domain OCT instruments) may be used to estimate the linear polarizability of a nanoparticle as a function of wavelength. The polarizability fully determines the elastic scattering properties of the nanoparticle provided that the particle is small enough to be characterized by a point polarizability. By measuring the polarizability, information regarding the particle shape, size, orientation, and material is obtained, suggesting applications in nanoparticle discrimination and characterization.

The main instrument modification over, for example, a high NA Fourier-domain OCT system is the inclusion of a vector-beam shaper. The beam shaper analyzed here is piecewise constant over the lens aperture and has a binary transmittance profile, leading to a simple potential realization with half-wave plates and aperture stops. There is also considerable flexibility in modifying this beam shaper, as all that is required is the creation of diverse instrument PSFs [calculated according to Eq. (14)] across the polarizability components.

The elements of the polarizability and the nanoparticle location are estimated from the collected data. The estimation procedure is a physically based algorithm found

by numerically solving the system inverse problem. The computational efficiency and stability of the estimation algorithm are aided by an approximation to the forward model and the fact that coherent detection means the system responds linearly to the polarizability elements. The inversion includes an iterative search method across the three nanoparticle position parameters, and numerical simulations show that the result is robust to both noise and focal plane uncertainty.

The proposed system is based on coherent detection, which means that it is not directly applicable to incoherent signals, such as fluorescence. However, harmonic generation, e.g., second-harmonic generation (SHG), is a coherent nonlinear process, and interferometric SHG imaging has been demonstrated [76,77]. As such, the measurement methodology described here can possibly be generalized to harmonic generation measurements. This would provide additional nanoparticle characterization possibilities and an alternative contrast mechanism.

ACKNOWLEDGMENTS

REFERENCES

1. V. Rotello, ed., *Nanoparticles: Building Blocks for Nanotechnology* (Springer, 2003).
2. G. Schmid, ed., *Nanoparticles: From Theory to Application* (Wiley, 2004).
3. D. Thassu, M. Deleers, and Y. Pathak, eds., *Nanoparticle Drug Delivery Systems* (Informa Healthcare, 2007).
4. K. Kalantar-Zadeh and B. Fry, *Nanotechnology-Enabled Sensors* (Springer, 2007).
5. J. W. Bulte and M. Modo, eds., *Nanoparticles in Biomedical Imaging* (Springer, 2008).
6. G. E. Fryxell and G. Cao, eds., *Environmental Applications of Nanomaterials: Synthesis, Sorbents and Sensors* (Imperial College, 2007).
7. E. Fritsch, E. Gaillou, B. Rondeau, A. Barreau, D. Albertini, and M. Ostroumov, "The nanostructure of fire opal," J. Non-Cryst. Solids **352**, 3957–3960 (2006).
8. D. Jembrih-Simbürger, C. Neelmeijer, O. Schalm, P. Fredrickx, M. Schreiner, K. De Vis, M. Mäder, D. Schryvers, and J. Caen, "The colour of silver stained glass—analytical investigations carried out with XRF, SEM/EDX, TEM and IBA," J. Anal. At. Spectrom. **17**, 321–328 (2002).
9. D. R. Smith, J. B. Pendry, and M. C. K. Wiltshire, "Metamaterials and negative refractive index," Science **305**, 788–792 (2004).
10. R. W. Ziolkowski and N. Engheta, eds., *Metamaterials: Physics and Engineering Explorations* (Wiley, 2006).
11. P. Mühlschlegel, H.-J. Eisler, O. J. F. Martin, B. Hecht, and D. W. Pohl, "Resonant optical antennas," Science **308**, 1607–1609 (2005).
12. J. Aaron, E. de la Rosa, K. Travis, N. Harrison, J. Burt, M. José-Yacamán, and K. Sokolov, "Polarization microscopy with stellated gold nanoparticles for robust, *in-situ* monitoring of biomolecules," Opt. Express **16**, 2153–2167 (2008).
13. J. J. Mock, M. Barbic, D. R. Smith, D. A. Schultz, and S. Schultz, "Shape effects in plasmon resonance of individual colloidal silver nanoparticles," J. Chem. Phys. **116**, 6755–6759 (2002).
14. J. Nelayah, M. Kociak, O. Stéphan, F. J. García de Abajo, M. Tence, L. Henrard, D. Taverna, I. Pastoriza-Santos, L. Liz-Marzán, and C. Colliex, "Mapping surface plasmons on a single metallic nanoparticle," Nat. Phys. **3**, 348–353 (2007).
15. H. C. van de Hulst, *Light Scattering by Small Particles* (Dover, 1981).
16. B. T. Draine and P. J. Flatau, "Discrete-dipole approximation for scattering calculations," J. Opt. Soc. Am. A **11**, 1491–1499 (1994).
17. J. Jin, *The Finite Element Method in Electromagnetics*, 2nd ed. (Wiley, 2002).
18. B. K. Canfield, S. Kujala, K. Laiho, K. Jefimovs, J. Turunen, and M. Kauranen, "Chirality arising from small defects in gold nanoparticle arrays," Opt. Express **14**, 950–955 (2006).
19. D. Gabor and W. P. Goss, "Interference microscope with total wavefront reconstruction," J. Opt. Soc. Am. **56**, 849–858 (1966).
20. D. Huang, E. A. Swanson, C. P. Lin, J. S. Schuman, W. G. Stinson, W. Chang, M. R. Hee, T. Flotte, K. Gregory, C. A. Puliafito, and J. G. Fujimoto, "Optical coherence tomography," Science **254**, 1178–1181 (1991).
21. M. E. Brezinski, *Optical Coherence Tomography: Principles and Applications* (Academic, 2006).
22. F. V. Ignatovich and L. Novotny, "Real-time and background-free detection of nanoscale particles," Phys. Rev. Lett. **96**, 013901 (2006).
23. C. L. Jahncke, H. D. Hallen, and M. A. Paesler, "Nano-Raman spectroscopy and imaging with a near-field scanning optical microscope," J. Raman Spectrosc. **27**, 579–586 (1996).
24. M. H. Nayfeh, O. Akcakir, G. Belomoin, N. Barry, J. Therrien, and E. Gratton, "Second harmonic generation in microcrystallite films of ultrasmall Si nanoparticles," Appl. Phys. Lett. **77**, 4086–4088 (2000).
25. T. Basché, W. E. Moerner, M. Orrit, and U. P. Wild, *Single-Molecule Optical Detection, Imaging and Spectroscopy* (VCH, 1997).
26. H. H. Barrett and K. Myers, *Foundations of Image Science* (Wiley-Interscience, 2003).
27. J. F. de Boer and T. E. Milner, "Review of polarization sensitive optical coherence tomography and Stokes vector determination," J. Biomed. Opt. **7**, 359–371 (2002).
28. T. Colomb, F. Dürr, E. Cuche, P. Marquet, H. G. Limberger, R.-P. Salathé, and C. Depeursinge, "Polarization microscopy by use of digital holography: Application to optical-fiber birefringence measurements," Appl. Opt. **44**, 4461–4469 (2005).
29. Y. L. Kim, Y. Liu, R. K. Wali, H. K. Roy, M. J. Goldberg, A. K. Kromin, K. Chen, and V. Backman, "Simultaneous measurement of angular and spectral properties of light scattering for characterization of tissue microarchitecture and its alteration in early precancer," IEEE J. Sel. Top. Quantum Electron. **9**, 243–256 (2003).
30. M. Mujat, E. Baleine, and A. Dogariu, "Interferometric imaging polarimeter," J. Opt. Soc. Am. A **21**, 2244–2249 (2004).
31. R. J. Ober, S. Ram, and E. S. Ward, "Localization accuracy in single-molecule microscopy," Biophys. J. **86**, 1185–1200 (2004).
32. S. Ram, E. S. Ward, and R. J. Ober, "Beyond Rayleigh's criterion: A resolution measure with application to single-molecule microscopy," Proc. Natl. Acad. Sci. U.S.A. **103**, 4457–4462 (2006).
33. A. Yildiz, J. N. Forkey, S. A. McKinney, T. Ha, Y. E. Goldman, and P. R. Selvin, "Myosin V walks hand-over-hand: Single fluorophore imaging with 1.5-nm localization," Science **300**, 2061–2065 (2003).
34. W. Rechberger, A. Hohenau, A. Leitner, J. R. Krenn, B. Lamprecht, and F. R. Aussenegg, "Optical properties of two interacting gold nanoparticles," Opt. Commun. **220**, 137–141 (2003).
35. M. A. van Dijk, A. L. Tchebotareva, M. Orrit, M. Lippitz, S. Berciaud, D. Lasne, L. Cognet, and B. Lounis, "Absorption and scattering microscopy of single metal nanoparticles," Phys. Chem. Chem. Phys. **8**, 3486–3495 (2006).

36. M. Artemyev, D. Kisiel, S. Abmiotko, M. N. Antipina, G. B. Khomutov, V. V. Kislov, and A. A. Rakhnyanskaya, "Self-organized highly luminescent CdSe nanorod-DNA complexes," J. Am. Chem. Soc. **126**, 10594–10597 (2004).

37. C. Sönnichsen and A. P. Alivisatos, "Gold nanorods as novel nobleaching plasmon-based orientation sensors for polarized single-particle microscopy," Nano Lett. **5**, 301–304 (2005).

38. A. V. Failla, H. Qian, H. Qian, A. Hartschuh, and A. J. Meixner, "Orientation imaging of subwavelength Au particles with higher order laser modes," Nano Lett. **6**, 1374–1378 (2006).

39. A. V. Failla, S. Jäger, T. Züchner, M. Steiner, and A. J. Meixner, "Topology measurements of metal nanoparticles with 1nm accuracy by confocal interference scattering microscopy," Opt. Express **15**, 8532–8542 (2007).

40. D. Haefner, S. Sukhov, and A. Dogariu, "Stochastic scattering polarimetry," Phys. Rev. Lett. **100**, 043901 (2008).

41. S. Sukhov, D. Haefner, and A. Dogariu, "Stochastic sensing of relative aniostropic polarizabilities," Phys. Rev. A **77**, 043820 (2008).

42. F. Kulzer and M. Orrit, "Single-molecule optics," Annu. Rev. Phys. Chem. **55**, 585–611 (2004).

43. S. Quabis, R. Dorn, and G. Leuchs, "Generation of a radially polarized doughnut mode of high quality," Appl. Phys. B **81**, 597–600 (2005).

44. K. C. Toussaint Jr., S. Park, J. E. Jureller, and N. F. Scherer, "Generation of optical vector beams with a diffractive optical element interferometer," Opt. Lett. **30**, 2846–2848 (2005).

45. M. A. A. Neil, F. Massoumian, R. Juškaitis, and T. Wilson, "Method for the generation of arbitrary complex vector wave fronts," Opt. Lett. **27**, 1929–1931 (2002).

46. A. F. Abouraddy and K. C. Toussaint, Jr., "Three-dimensional polarization control in microscopy," Phys. Rev. Lett. **96**, 153901 (2006).

47. M. R. Beversluis, L. Novotny, and S. J. Stranick, "Programmable vector point-spread function engineering," Opt. Express **14**, 2650–2656 (2006).

48. M. Prummer, B. Sick, B. Hecht, and U. P. Wild, "Three-dimensional optical polarization tomography of single molecules," J. Chem. Phys. **118**, 9824–9829 (2003).

49. J. T. Fourkas, "Rapid determination of the three-dimensional orientation of single molecules," Opt. Lett. **26**, 211–213 (2001).

50. B. Sick, B. Hecht, and L. Novotny, "Orientational imaging of single molecules by annular illumination," Phys. Rev. Lett. **85**, 4482–4485 (2000).

51. M. A. Lieb, J. M. Zavislan, and L. Novotny, "Single-moleculeorientations determined by direct emission pattern imaging," J. Opt. Soc. Am. B **21**, 1210–1215 (2004).

52. L. Novotny, M. R. Beversluis, K. S. Youngworth, and T. G. Brown, "Longitudinal field modes probed by single molecules," Phys. Rev. Lett. **86**, 5251–5254 (2001).

53. A. P. Bartko and R. M. Dickson, "Three-dimensional orientations of polymer-bound single molecules," J. Phys. Chem. B **103**, 3051–3056 (1999).

54. A. P. Bartko and R. M. Dickson, "Imaging three-dimensional single molecule orientations," J. Phys. Chem. B **103**, 11237–11241 (1999).

55. M. Böhmer and J. Enderlein, "Orientation imaging of single molecules by wide-field epifluorescence microscopy," J. Opt. Soc. Am. B **20**, 554–559 (2003).

56. E. Toprak, J. Enderlein, S. Syed, S. A. McKinney, R. G. Petschek, T. Ha, Y. E. Goldman, and P. R. Selvin, "Defocused orientation and position imaging (DOPI) of myosin V," Proc. Natl. Acad. Sci. U.S.A. **103**, 6495–6499 (2006).

57. R. Hassey, E. J. Swain, N. I. Hammer, D. Venkataraman, and M. D. Barnes, "Probing the chiroptical response of a single molecule," Science **314**, 1437–1439 (2006).

58. D. Patra, I. Gregor, J. Enderlein, and M. Sauer, "Defocused imaging of quantum-dot angular distribution of radiation," Appl. Phys. Lett. **87**, 101103 (2005).

59. B. J. Davis, A. K. Swan, M. S. Ünlü, W. C. Karl, B. B. Goldberg, J. C. Schotland, and P. S. Carney, "Spectral self-interference microscopy for low-signal nanoscale axial imaging," J. Opt. Soc. Am. A **24**, 3587–3599 (2007).

60. B. J. Davis, S. C. Schlachter, D. L. Marks, T. S. Ralston, S. A. Boppart, and P. S. Carney, "Nonparaxial vector-field modeling of optical coherence tomography and interferometric synthetic aperture microscopy," J. Opt. Soc. Am. A **24**, 2527–2542 (2007).

61. R. Leitgeb, C. K. Hitzenberger, and A. F. Fercher, "Performance of Fourier domain vs. time domain optical coherence tomography," Opt. Express **11**, 889–894 (2003).

62. Y. Zhao, Z. Chen, C. Saxer, S. Xiang, J. F. de Boer, and J. S. Nelson, "Phase-resolved optical coherence tomography and optical Doppler tomography for imaging blood flow in human skin with fast scanning speed and high velocity sensitivity," Opt. Lett. **25**, 114–116 (2000).

63. B. J. Davis, T. S. Ralston, D. L. Marks, S. A. Boppart, and P. S. Carney, "Autocorrelation artifacts in optical coherence tomography and interferometric synthetic aperture microscopy," Opt. Lett. **32**, 1441–1443 (2007).

64. B. Richards and E. Wolf, "Electromagnetic diffraction in optical systems. II. Structure of the image field in an aplanatic system," Proc. R. Soc. London, Ser. A **253**, 358–379 (1959).

65. I. J. Cooper, M. Roy, and C. J. R. Sheppard, "Focusing of pseudoradial polarized beams," Opt. Express **13**, 1066–1071 (2005).

66. P. Török, P. Varga, Z. Laczik, and G. R. Booker, "Electromagnetic diffraction of light focused through a planar interface between materials of mismatched refractive indices: An integral representation," J. Opt. Soc. Am. A **12**, 325–332 (1995).

67. R. J. Potton, "Reciprocity in optics," Rep. Prog. Phys. **67**, 717–754 (2004).

68. D. Patra, I. Gregor, and J. Enderlein, "Image analysis of defocused single-molecule images for three-dimensional molecule orientation studies," J. Phys. Chem. A **108**, 6836–6841 (2004).

69. P. N. Butcher and D. Cotter, *The Elements of Nonlinear Optics* (Cambridge U. Press, 1990), Chap. 5.2, pp. 131–134.

70. S. M. Kay, *Fundamentals of Statistical Signal Processing: Estimation Theory* (Prentice-Hall, 1993).

71. J. A. Nelder and R. Mead, "A simplex method for function minimization," Comput. J. **7**, 308–313 (1965).

72. W. H. Press, S. A. Teukolsky, W. T. Vetterling, and B. P. Flannery, *Numerical Recipes: The Art of Scientific Computing*, 3rd ed. (Cambridge U. Press, 2007), Chap. 10.5, pp. 502–507.

73. M. Leutenegger, R. Rao, R. A. Leitgeb, and T. Lasser, "Fast focus field calculations," Opt. Express **14**, 11277–11291 (2006).

74. I. J. Cooper, C. J. R. Sheppard, and M. Roy, "The numerical integration of fundamental diffraction integrals for converging polarized spherical waves using a two-dimensional form of Simpson's 1/3 rule," J. Mod. Opt. **52**, 1123–1134 (2005).

75. E. De Castro and C. Morandi, "Registration of translated and rotated images using finite Fourier transforms," IEEE Trans. Pattern Anal. Mach. Intell. **PAMI-9**, 700–705 (1987).

76. S. Yazdanfar, L. H. Laiho, and P. T. C. So, "Interferometric second harmonic generation microscopy," Opt. Express **12**, 2739–2745 (2004).

77. B. E. Applegate, C. Yang, A. M. Rollins, and J. A. Izatt, "Polarization-resolved second-harmonic-generation optical coherence tomography in collagen," Opt. Lett. **29**, 2252–2254 (2004).